




High-speed, low-voltage, low-bit-energy silicon photonic crystal slow-light modulator with impedance-engineered distributed electrodes: supplement

KEISUKE KAWAHARA,^{1,*}  TAI TSUCHIZAWA,² NORITSUGU YAMAMOTO,² YURIKO MAEGAMI,²  KOJI YAMADA,² SHINSUKE HARA,³ AND TOSHIHIKO BABA¹ 

¹*Department of Electrical and Computer Engineering, Yokohama National University, Yokohama, 240-8501, Japan*

²*National Institute of Advanced Industrial Science and Technology (AIST), Tsukuba, 305-8568, Japan*

³*National Institute of Information and Communications Technology (NICT), Koganei, 184-8795, Japan*

*keisuke@ieee.org

This supplement published with Optica Publishing Group on 28 August 2024 by The Authors under the terms of the [Creative Commons Attribution 4.0 License](https://creativecommons.org/licenses/by/4.0/) in the format provided by the authors and unedited. Further distribution of this work must maintain attribution to the author(s) and the published article's title, journal citation, and DOI.

Supplement DOI: <https://doi.org/10.6084/m9.figshare.26591410>

Parent Article DOI: <https://doi.org/10.1364/OPTICA.531372>

0.87 V, 59 fJ/bit, 64 Gbps Silicon Photonic Crystal Slow-Light Modulator With Impedance-Engineered Distributed Electrodes:
SUPPLEMENTAL DOCUMENT

1. Derivation of Eqs. (1)–(3)

This section provides the derivation of Eqs. (1)–(3), which is based on the analysis of distributed amplifiers, which is well known in the field of electronics [1]. An interesting fact is that the distributed electrodes in optical modulators and the gate lines in distributed amplifiers are modeled as the same unit cell circuit. Thus, most analytical formulas and theoretical insights can be diverted to optical modulators. Assuming that the coplanar line is lossless, the unit cell model of a distributed electrode circuit is shown in Fig. S1, and Z_0 is given by

$$Z_0 = \sqrt{\frac{j\omega L_H}{j\omega C_H + \frac{j\omega C_{pn}}{1 + j\omega R_{pn}C_{pn}}}}. \#(S1)$$

Assuming $\omega R_{pn}C_{pn} \ll 1$, Eq. (S1) is approximated by

$$Z_0 \approx \sqrt{\frac{L_H}{C_H + C_{pn}}}. \#(S2)$$

In the same manner as above, $\alpha_{RF} + j\beta_{RF}$ is given by

$$\begin{aligned} \alpha_{RF} + j\beta_{RF} &= \frac{1}{l_U} \sqrt{j\omega L_H \left(j\omega C_H + \frac{j\omega C_{pn}}{1 + j\omega R_{pn}C_{pn}} \right)} \\ &\approx \frac{1}{l_U} \sqrt{-\omega^2 L_H (C_H + C_{pn} - j\omega C_{pn}^2 R_{pn})} \\ &\approx \frac{1}{l_U} \left[j\omega \sqrt{L_H (C_H + C_{pn})} \cdot \left(1 - \frac{j\omega L_H C_{pn}^2 R_{pn}}{2L_H (C_H + C_{pn})} \right) \right] \\ &= \frac{1}{l_U} \left(\frac{\omega^2 R_{pn} C_{pn}^2 Z_0}{2} + j\omega \sqrt{L_H (C_H + C_{pn})} \right). \#(S3) \end{aligned}$$

Assuming that the roll-off due to phase mismatch is sufficiently small, the normalized electro-optic frequency response $G_{EO}(f)$ is determined by the RC response $G_{RC}(f)$ and the mean propagation loss for each segment, as follows:

$$G_{EO}(f) = G_{RC}(f) \cdot \frac{1}{N} \sum_{n=1}^N e^{-(n-1)\alpha_{RF}l_U}. \#(S4)$$

Applying the formula for the sum of a sequence of equal ratios $a(1 - r^n)/(1 - r)$ with an initial term a and ratio r , Eq. (S4) is simplified as

$$G_{EO}(f) = \left| \frac{1}{1 + j\omega R_{pn}C_{pn}} \right| \cdot \frac{1 - e^{-N\alpha_{RF}l_U}}{N(1 - e^{-\alpha_{RF}l_U})}. \#(S5)$$

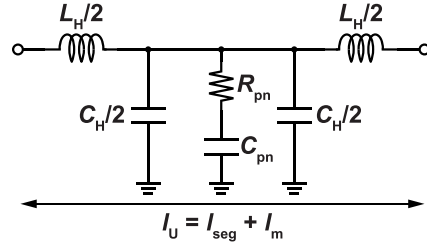


Fig. S1. Circuit model of the unit cell of a distributed electrode.

2. Analysis of Distributed Electrodes as Periodic Transmission Lines

In the primary document, each transmission line in the distributed electrode is approximated by a lumped network as shown in Fig. 1(d). On the other hand, when the inductive elements inserted between the segmented phase shifters are transmission lines such as coplanar waveguides, the distributed electrode can be treated as a periodic transmission line. In this case, the behavior at higher frequencies, where the lumped constant approximation does not hold, becomes clear, providing more insight and design guidelines.

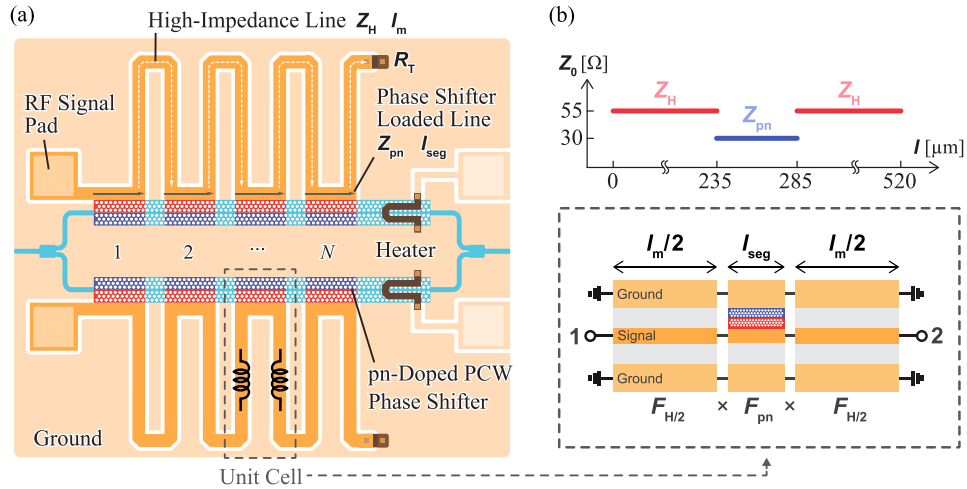


Fig. S2. Distributed electrode Si photonic crystal waveguide slow-light modulator. (a) Schematic structure. (b) Unit cell of the distributed electrode as a periodic transmission line.

Figure S2 demonstrates the unit cell of the electrode as a symmetric two-port network. The electrode can be considered a periodic waveguide with a low-impedance section of Z_{pn} and a high-impedance section of Z_H . The phase shift of the high- and low-impedance sections are denoted by $\theta_1 = \omega n_1 I_m / c$ and $\theta_2 = \omega n_2 I_{seg} / c$, respectively, with RF refractive indices of n_1 and n_2 for the inserted transmission lines and phase shifter electrode, respectively. Supposing that these transmission lines are lossless for simplicity, the ABCD parameters of the unit cell are derived as follows:

$$F_U = \begin{bmatrix} A & B \\ C & D \end{bmatrix} = F_{H/2} \times F_{pn} \times F_{H/2}$$

$$= \begin{bmatrix} \cos \frac{\theta_1}{2} & jZ_H \sin \frac{\theta_1}{2} \\ \frac{j}{Z_H} \sin \frac{\theta_1}{2} & \cos \frac{\theta_1}{2} \end{bmatrix} \begin{bmatrix} \cos \theta_2 & jZ_{pn} \sin \theta_2 \\ \frac{j}{Z_{pn}} \sin \theta_2 & \cos \theta_2 \end{bmatrix} \begin{bmatrix} \cos \frac{\theta_1}{2} & jZ_H \sin \frac{\theta_1}{2} \\ \frac{j}{Z_H} \sin \frac{\theta_1}{2} & \cos \frac{\theta_1}{2} \end{bmatrix} \#(S6)$$

The input impedance of the periodic circuit is computed as the image impedance Z_{image} given by

$$Z_{\text{image}} = \sqrt{\frac{AB}{CD}}$$

$$= \sqrt{Z_H^2 \frac{2jZ_H Z_{\text{pn}} \sin \frac{\theta_1}{2} \cos \frac{\theta_1}{2} \cos \theta_2 - jZ_H^2 \sin^2 \frac{\theta_1}{2} \sin \theta_2 + jZ_{\text{pn}}^2 \cos^2 \frac{\theta_1}{2} \sin \theta_2}{2jZ_H Z_{\text{pn}} \sin \frac{\theta_1}{2} \cos \frac{\theta_1}{2} \cos \theta_2 + jZ_H^2 \cos^2 \frac{\theta_1}{2} \sin \theta_2 - jZ_{\text{pn}}^2 \sin^2 \frac{\theta_1}{2} \sin \theta_2}} \quad \#(S7)$$

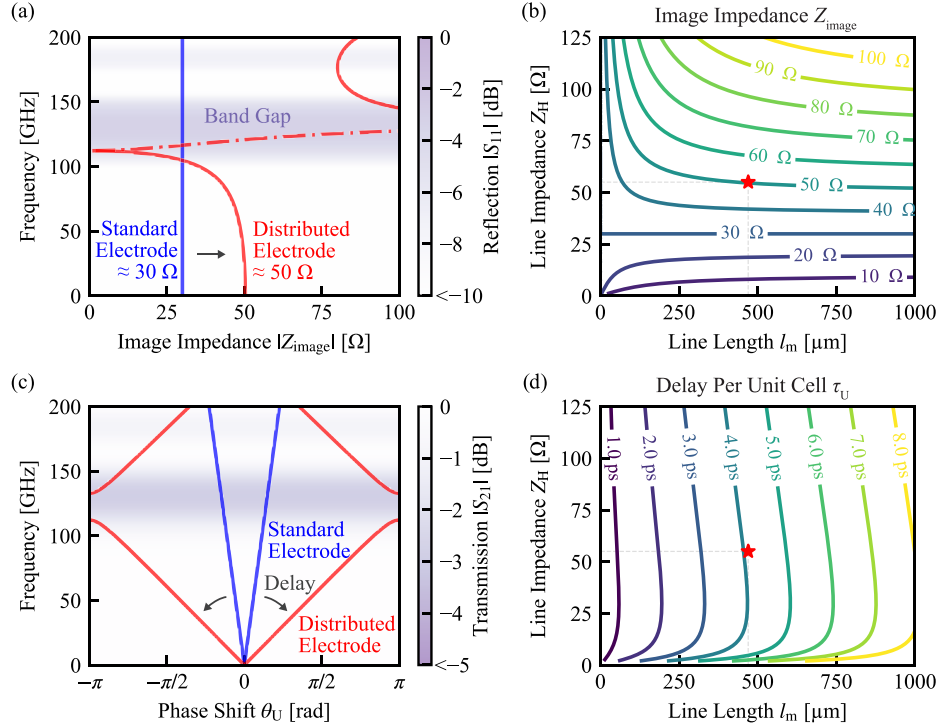


Fig. S3. Analysis results of distributed electrodes. (a) Frequency response of the image impedance per unit cell Z_{image} and reflection coefficient $|S_{11}|$ at $l_m = 470 \mu\text{m}$, $l_{\text{seg}} = 50 \mu\text{m}$, $n_1 = 2.2$, $n_2 = 3.4$, $Z_H = 55 \Omega$, $Z_{\text{pn}} = 30 \Omega$, and $N = 3$. (b) Computed image impedance for various Z_H and l_m . (c) Frequency response of the phase shifter per unit cell θ_U and transmission coefficient $|S_{21}|$ in the above parameters. (d) Computed delay per unit cell τ_U for various Z_H and l_m .

Figure S3(a) presents the computed Z_{image} and $|S_{11}|$ for $l_m = 470 \mu\text{m}$, $l_{\text{seg}} = 50 \mu\text{m}$, $n_1 = 2.2$, $n_2 = 3.4$, $Z_H = 55 \Omega$, $Z_{\text{pn}} = 30 \Omega$, and $N = 3$, which relate to the design parameters of the prototype device. The solid line and chain line denote the resistive and reactive components of the impedance, respectively. While the input impedance of the standard electrode is constant at all frequencies, the distributed electrode is characterized by frequency dependence owing to its periodicity. The distributed electrode demonstrates a reactive impedance near 120 GHz and generates a bandgap due to the Bragg reflection that arises when the RF wavelength approaches the unit length. This bandgap restrains the operation of the waveguide; hence, the distributed electrodes must be used at frequencies adequately less than the Bragg frequency for RF waves. This bandgap can effortlessly be moved to higher frequencies by raising the N and shortening the l_{seg} and l_m . In the prototype device, l_{seg} was set to short enough ($\approx 50 \mu\text{m}$) so that the Bragg

frequency is sufficiently high and the EO phase mismatch within each segment is negligibly small. When the RF frequency is adequately low ($\omega \rightarrow 0$), the Z_{image} is estimated as follows:

$$Z_{\text{image}}|_{\omega \rightarrow 0} \approx \sqrt{Z_H Z_{\text{pn}} \cdot \frac{Z_H \theta_1 + Z_{\text{pn}} \theta_2}{Z_H \theta_2 + Z_{\text{pn}} \theta_1}}. \#(S8)$$

The phase shift per unit cell, namely, θ_U , is computed from the ABCD parameters by the following:

$$\begin{aligned} \theta_U(\omega) &= \arccos \frac{A + D}{2} \\ &= \arccos \left[\cos \theta_1 \cos \theta_2 - \frac{1}{2} \left(\frac{Z_H}{Z_{\text{pn}}} + \frac{Z_{\text{pn}}}{Z_H} \right) \sin \theta_1 \sin \theta_2 \right]. \#(S9) \end{aligned}$$

Figure S3(b) presents the computed Z_{image} for several Z_H and l_m . In the CMOS technology, the Z_H and l_m are restricted up to 125 Ω and 1,000 μm , considering the RF losses. In spite of this constraint, the Z_{image} demonstrates a high design flexibility reaching 100 Ω . The red star signifies the design point of the prototype modulator with $Z_{\text{image}} = 50 \Omega$. This impedance value is higher than that of regular Si modulators. Figure 3(c) presents the computed and $|S_{21}|$. The distributed electrode operates as a waveguide below 100 GHz, and its phase shift is substantially greater than that of the normal electrode. Figure S3(d) exhibits the delay per unit cell, $\tau_U = \theta_U/\omega$, for several Z_H and l_m . When the ratio of Z_H to Z_{pn} rises, the propagation speed of the RF signal decreases. This distinct performance is identical to that of a slow-wave transmission line [2], and θ_U is more than or equal to $\theta_1 + \theta_2$. In our proposal, the slow light has a group delay of 4.3 ps per unit cell, so the design point signified by the red star guarantees phase matching. An important design consideration is that the design parameters (Z_H and l_m) of a coplanar waveguide are uniquely determined to simultaneously satisfy the impedance matching and EO phase matching requirements. A comparison of Figs. S3(b) and (d) reveal that impedance and delay are extremely independent. Therefore, we can determine the Z_H and l_m that satisfy the target impedance and target delay from Figs. S3(b) and (d) based on Eqs. (S8) and (S9). That is, given a specific l_{seg} , n_g , and Z_{pn} , there is only one point where Z_H and l_m satisfy the target Z_{image} and τ_U as indicated by the red star. Once the Z_H is determined, the wiring width and gap of the coplanar waveguide are then determined.

3. Lumped Implementation of Distributed Electrodes

As reported in the previous study, distributed electrodes can also be implemented using lumped inductors such as spiral inductors [3]. This section presents an analysis of distributed electrodes when each element is modeled as a complete lumped element as shown in Fig. S4. The analytical model is very similar to, but different from, that described in the primary document. The main difference is that the physical length of the inductive element, l_m , is not defined. The analysis in this section is based on the analysis of a lossy LC ladder circuit also known as a constant- k filter [4]. For the constant- k filter, the electrode impedance is expressed as an image impedance instead of the characteristic impedance, as follows:

$$Z_{\text{image}} = \sqrt{\frac{L_H}{C_{\text{pn}}} \left[1 - \left(\frac{\omega}{\omega_C} \right)^2 \right]}. \#(S10)$$

where ω_C represents the cut-off frequency of the filter defined by

$$\omega_C = \frac{2}{\sqrt{L_H C_{\text{pn}}}}. \#(S11)$$

The image attenuation function A_{RF} is given by

$$A_{\text{RF}} = \frac{\left(\frac{\omega_C}{\omega_{\text{pn}}}\right) X_k^2}{\sqrt{1 - \left[1 - \left(\frac{\omega_C}{\omega_{\text{pn}}}\right)^2\right] X_k^2}}, \#(\text{S12})$$

where

$$\omega_{\text{pn}} = \frac{1}{R_{\text{pn}} C_{\text{pn}}}, \#(\text{S13})$$

$$X_k = \frac{\omega}{\omega_C}. \#(\text{S14})$$

Similar to Eq. (S4), the normalized EO gain is given by

$$G_{\text{EO}}(f) = G_{\text{RC}}(f) \cdot \frac{1}{N} \sum_{n=1}^N e^{-(n-1)A_{\text{RF}}}$$

$$= \left| \frac{1}{1 + j\omega R_{\text{pn}} C_{\text{pn}}} \right| \cdot \frac{1 - e^{-NA_{\text{RF}}}}{N(1 - e^{-A_{\text{RF}}})}. \#(\text{S15})$$

L_{H} can be determined to achieve target Z_{image} at $\omega = 0$ from Eq. (S10). Fig. S5 shows the calculated achievable $f_{3\text{dB}}$ for several target impedances. The RF loss increases at higher impedance due to the large inductance. As with the case of using transmission lines, slow light reduces the required inductance and draws out the device's intrinsic bandwidth.

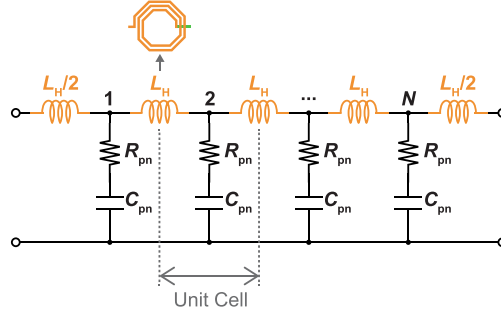


Fig. S4. Lumped circuit model of the distributed electrode.

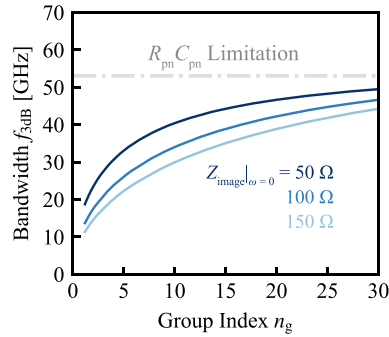


Fig. S5. Achievable $f_{3\text{dB}}$ in the lumped implementation of the distributed electrode modulator at $R_{\text{pn}} = 240 \, \Omega$ and $C_{\text{pn}} = 12.5 \, \text{fF}$.

4. Characterization of the Coplanar Waveguides

The coplanar waveguide used in the prototype modulator includes a dummy block at the bottom of the transmission line to eliminate irregularities in the metal and reduce high-frequency loss as shown in Fig. S6(a). We verified the effect of the dummy block by S-parameter measurements. Figure S6(b) and (c) shows micrographs of the test devices. We used Keysight's PNA-X N5247B 4-port network analyzer calibrated by the line-reflect-reflect-match method using FormFactor's WinCal software. The propagation constants $\gamma = \alpha + j\beta$ of the transmission lines were obtained from the measured S -parameters of open dummy, through dummy, and transmission lines with different lengths (100 μm , 200 μm , 650 μm) by using multiline through-reflect-line calibration [5, 6]. The quality factor, Q , was obtained by

$$Q = \frac{\beta}{2\alpha} \#(S16)$$

Figure S7 shows the measured γ and Q . The black and red lines correspond to with and without dummies. The high-frequency losses were suppressed by blocking the dummies. This is due to the elimination of the unevenness of the electrode and the reduction of parasitic resistance. The phase constant was almost unchanged regardless of the presence or absence of dummies. The quality factor increased from 7 to 9 at 40 GHz by dummy blocking. The reduction of parasitic resistance in the coplanar transmission line suppresses the bandwidth limitation due to RF losses in distributed electrodes.

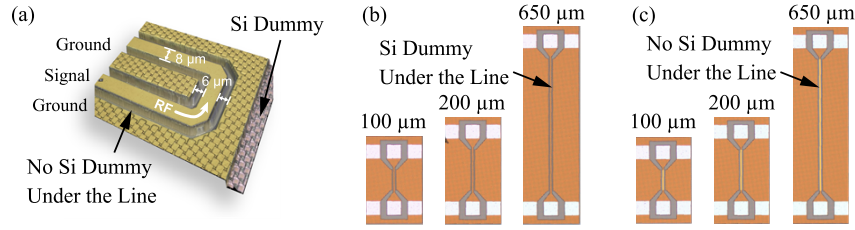


Fig. S6. Micrograph of the test devices of the electrode. (a) Coplanar waveguide with Si dummy under the line. (b) Coplanar waveguide without Si dummy under the line. (c) Laser micrograph of the coplanar waveguide in the prototype modulator.

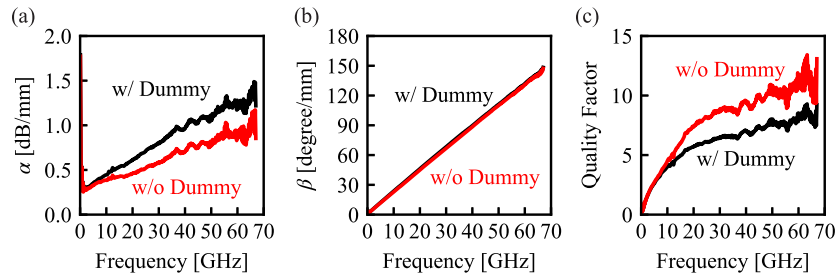


Fig. S7. Measured propagation constants and quality factors of the coplanar waveguides with and without Si dummies. (a) Attenuation constant. (b) Phase constant. (c) Quality factor.

5. Group Index

We measured the group index, n_g , by a dispersion analyzer (Alnair Labs, CDA-2100) as shown in Fig. S8(a). Although the device under test differs from that described in the primary document, the PCW structure and shuttle process remain the same. The operation wavelength of the PCW shifted toward the longer wavelength by 3 nm compared to the device in the primary document due to the process variations. This study intentionally used a simple PCW without lattice shift that exhibited wavelength dependence in n_g ranging from 25 to 70. This

strong dispersion allows for experiments at various n_g by changing the laser wavelength, which helps in the evaluation of phase matching. We evaluated the modulator at the wavelength with the lowest optical loss, $n_g \approx 30$ at that wavelength. n_g of the prototype device was larger than the target value of $n_g = 20$ due to the reduced thickness of the silicon slab layer as noted in the primary document. While this improved the modulation efficiency, it also increased the optical loss and slightly worsened the EO phase matching. Fig. S8(b) shows the simulated EO frequency response at $n_g = 20$ and 30. For the prototype device ($n_g = 30$), the EO bandwidth is expected to drop to $f_{3dB} \approx 31$ GHz, but still maintains 64-Gbaud modulation capability. Better performance is expected by controlling manufacturing variation. In addition, lattice-shifted PCWs can be employed to cover the full C-band at a constant n_g for practical usages. The athermal operation using the lattice-shifted PCWs has already been experimentally demonstrated by our group [7]. The athermal operation will be possible in the proposed modulator by employing lattice-shifted PCWs.

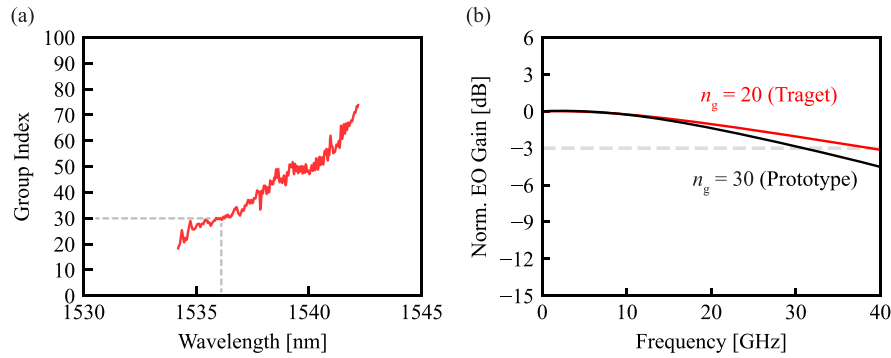


Fig. S8. (a) Measured n_g of the PCW. (b) Simulated EO frequency responses for $n_g = 20$ and 30.

References

1. Y. Ayasli, R. L. Mozzi, J. L. Vorhaus, *et al.*, "A Monolithic GaAs 1-13-GHz Traveling-Wave Amplifier," *IEEE Transactions on Microwave Theory and Techniques* **30**, 976–981 (1982).
2. S. Seki and H. Hasegawa, "Cross-tie slow-wave coplanar waveguide on semi-insulating GaAs substrates," *Electron. Lett.* **17**, 940–941 (1981).
3. D. M. Gill, W. M. J. Green, C. Xiong, *et al.*, "Distributed electrode Mach-Zehnder modulator with double-pass phase shifters and integrated inductors," *Opt. Express* **23**, 16857–16865 (2015).
4. J. B. Beyer, S. N. Prasad, R. C. Becker, *et al.*, "MESFET Distributed Amplifier Design Guidelines," *IEEE Trans. Microwave Theory Techn.* **32**, 268–275 (1984).
5. R. B. Marks, "A multiline method of network analyzer calibration," *IEEE Trans. Microwave Theory Techn.* **39**, 1205–1215 (1991).
6. <https://scikit-rf.readthedocs.io/en/latest/api/calibration/generated/skrf.calibration.calibration.NISTMultilineTRL.html>
7. H. C. Nguyen, N. Yazawa, S. Hashimoto, *et al.*, "Sub-100 μm Photonic Crystal Si Optical Modulators: Spectral, Athermal, and High-Speed Performance," *IEEE J. Sel. Top. Quantum Electron.* **19**, 127–137 (2013).